JOURNAL OF THEORETICAL
AND APPLIED MECHANICS
64, 3, pp. 217–229, Warsaw 2026
https://doi.org/10.15632/jtam-pl/225130

HYDROMECHANICAL DEGRADATION AND FATIGUE-LIKE DAMAGE MECHANISM OF SATURATED RED SANDSTONE SUBJECTED TO CYCLIC PORE-WATER PRESSURE

Wenjun ZHONG[1], Junzhe XU[2*], Ningbo HE[1]

[1] *China Anergy Group Third Engineering Bureau Co. Ltd., Chengdu, China*
[2] *School of Civil and Hydraulic Engineering, Chongqing University of Science and Technology, Chongqing, China*
[*]corresponding author, *2024206032@cqust.edu.cn*

Triaxial tests under 2 MPa confinement investigated saturated red sandstone degradation under cyclic pore-water pressure. A 0.3 MPa cyclic pressure reduces peak strength by 18.3 %. Deformation remains stable below 70 % of peak strength. Conversely, unstable fatigue damage accelerates post-eight cycles at 80 % stress. These results elucidate hydromechanical fatigue mechanisms, improving reservoir slope stability evaluations.

Keywords: saturated red sandstone; cyclic pore-water pressure; hydromechanical coupling; fatigue-like damage; energy dissipation.

1. Introduction

The long-term stability of reservoir bank slopes is a critical determinant for the safety of large-scale hydraulic infrastructure, such as the Three Gorges Reservoir (TGR) area in China (Yang *et al.*, 2025; He *et al.*, 2020). Unlike typical engineered slopes, reservoir banks are subjected to periodic water-level fluctuations driven by seasonal regulation and flood control operations. These fluctuations inevitably induce cyclic variations in the pore-water pressure within the submerged rock mass (Liao *et al.*, 2025). According to the principle of effective stress (Terzaghi, 1943), such hydraulic perturbations dynamically alter the stress state of the rock framework, acting as a recurring internal load. Distinct from external mechanical cyclic loading, this process is now recognized as a primary driver of hydraulic fatigue (Li *et al.*, 2023; Hu *et al.*, 2023). Such progressive deterioration continuously threatens the structural durability of bank slope rock masses.

Extensive research has established that water weakens sandstone through physical and chemical processes, such as the reduction of cementation strength, alteration of mineral surfaces, and promotion of subcritical crack growth (Wang *et al.*, 2026; Li *et al.*, 2025; Xu *et al.*, 2022). However, most existing studies have focused on two specific conditions:

1) monotonic water-weakening (Xuan *et al.*, 2025; Liang *et al.*, 2024), in which the degradation is time-dependent under constant hydraulic conditions,
2) dry-wet cycling (Wang *et al.*, 2023; Taheri *et al.*, 2016), which simulates the long-term weathering process over months or years.

While these studies explain long-term softening, they fail to capture the short-term, fatigue-like damage induced by frequent, transient pore-pressure pulses occurring within the rock mass while it sustains high gravitational shear stresses.

Recent investigations into hydraulic fracturing and deep-earth engineering have touched upon the effects of cyclic hydraulic pressure. For instance, Kendrick *et al.* (2024) and Chang *et al.* (2022) reported that cyclic pressurization accelerates microcrack initiation and alters failure modes. Similarly, energy-based analyses have highlighted that water–rock interaction enhances energy dissipation and localization during cyclic loading (Sun *et al.*, 2024; Li *et al.*, 2020). Nevertheless, a critical gap remains in the context of reservoir slope engineering. Most prior experiments utilized extremely high hydraulic pressures (aimed at fracturing) or focused on permeability evolution alone. The mechanisms by which low amplitude cyclic pore pressure couples with high static axial stress to induce fatigue failure remain systematically unexplored. These low amplitude cycles accurately reflect realistic reservoir fluctuations. Furthermore, the critical stress threshold governing the transition from stable deformation to unstable hydraulic damage requires deeper investigation (Sawicki & Mierczyński, 2015).

To bridge this gap, this study investigates the hydromechanical degradation of saturated red sandstone from the TGR area. The experimental design strictly mimics the in situ stress and hydraulic conditions of shallow landslides in the TGR: a constant confining pressure of 2 MPa (simulating the overburden stress of a shallow sliding mass) and a cyclic pore-water pressure amplitude of 0.3 MPa (corresponding to the 30 m annual water-level regulation). By conducting triaxial compression tests combined with 20-cycle pore-pressure loading, this work aims to:

1) quantify the short-term strength reduction induced by reservoir-scale hydraulic fluctuations,
2) characterize the transition of deformation behaviors from stable hysteresis to nonlinear accumulation,
3) establish a residual-strain-based damage variable to elucidate the stress-dependent evolution mechanism.

The findings provide new theoretical insights into the "hydraulic fatigue" of reservoir rocks and offer a rigorous basis for evaluating the stability of bank slopes under complex hydromechanical coupling.

2. Materials and methods

2.1. Specimen preparation

The red sandstone blocks utilized in this study were collected from the hydro-fluctuation belt of the TGR area. The natural rock is characterized by a massive structure and a uniform dark red texture. All test specimens were cored from a single intact rock block to maximize initial material consistency. These cores were subsequently processed into standard cylinders with a diameter of 50 mm and a height of 100 mm (as shown in Fig. 1). This preparation strictly adhered to the guidelines established by the International Society for Rock Mechanics (ISRM) (Ulusay & Hudson, 2007). The machining precision was rigorously controlled to restrict diameter

Fig. 1. Red sandstone specimens processed into standard cylinders (50 mm × 100 mm) (He *et al.*, 2026).

deviation within 0.3 mm and limit end face non-parallelism to under 0.05 mm. Prior to testing, all specimens were oven-dried at 105 °C for 24 h to eliminate initial moisture content. Subsequently, the saturation process was conducted using the boiling-water saturation method for 48 h to ensure full saturation. Ultrasonic P wave velocity measurements and bulk density evaluations were conducted on all prepared dry specimens. Only those specimens exhibiting a P wave velocity deviation of less than three percent and nearly identical bulk densities were selected for the final testing phase. A subsequent boiling water saturation method was applied for 48 h to ensure complete fluid saturation before the triaxial loading.

2.2. Testing apparatus

Hydromechanical coupling tests were performed using the TFD-2000 microcomputer servo-controlled rock triaxial testing system. This high-stiffness apparatus is capable of independently controlling axial stress, confining pressure, and pore-water pressure. It has a maximum axial load capacity of 2000 kN and a maximum confining pressure of 140 MPa. The control precision is ±0.5 % for axial load and ±0.1 % for pore-water pressure. A high-speed data acquisition system recorded the axial stress, strain, and pore-water pressure synchronously at a sampling rate of 10 Hz, ensuring sufficient resolution to capture the deformation response during rapid hydraulic loading phases.

2.3. Experimental procedure

The testing protocol was designed to simulate the in situ stress conditions of reservoir bank slopes subjected to water-level fluctuations. The cyclic water pressure amplitude was set to 0.3–0 MPa, corresponding to the 30 m seasonal water-level regulation (175 m to 145 m) in the TGR. The specific testing stages were as follows (see Fig. 2):

1) A hydrostatic confining pressure σ_3 of 2 MPa was applied at a rate of 5 MPa/min to simulate the overburden pressure of a shallow landslide mass.
2) With the confining pressure held constant, the axial stress (σ_1) was loaded at 5 MPa/min to a target level. Three target stress levels were selected: 27.41 MPa, 31.98 MPa, and 36.55 MPa, corresponding to 60 %, 70 %, and 80 % of the saturated peak strength $\sigma_{\mathrm{peak}}^{\mathrm{sat}} =$ 45.69 MPa determined under a constant pore pressure of 0.3 MPa.
3) Under constant axial and confining stresses, a triangular waveform was employed to alternate the water pressure between 0 Mpa and 0.3 MPa at a rate of 0.01 MPa/min, simulating the water level dropping from 175 m to 145 m and then recovering to 175 m. This cycle was repeated 20 times for each specimen to evaluate fatigue-like degradation behavior.

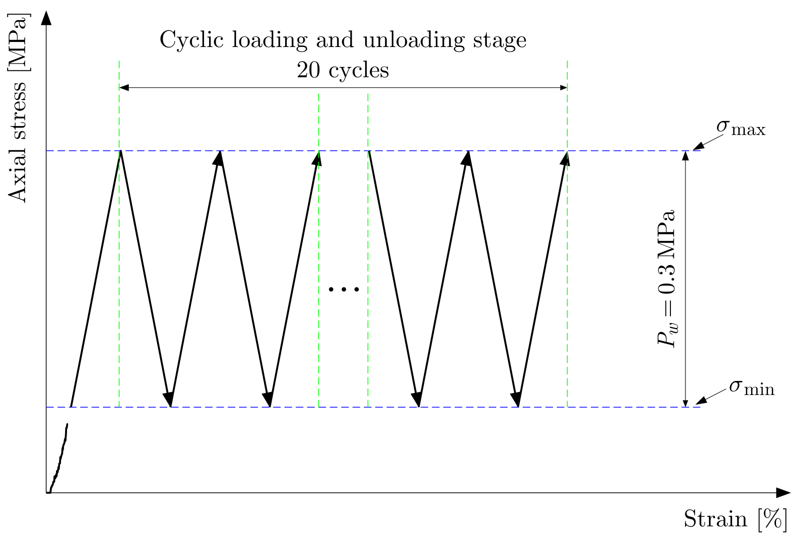

Fig. 2. Schematic diagram of the stress path and cyclic water pressure loading scheme.

3. Test results and analysis

3.1. Degradation of short-term mechanical properties

To establish a baseline for cyclic testing, the mechanical response of the red sandstone was first evaluated under monotonic triaxial compression at a confining pressure of 2 MPa. Figure 3 compares the stress-strain behavior between the dry ($P_w = 0$ MPa) and saturated-pressurized ($P_w = 0.3$ MPa) states.

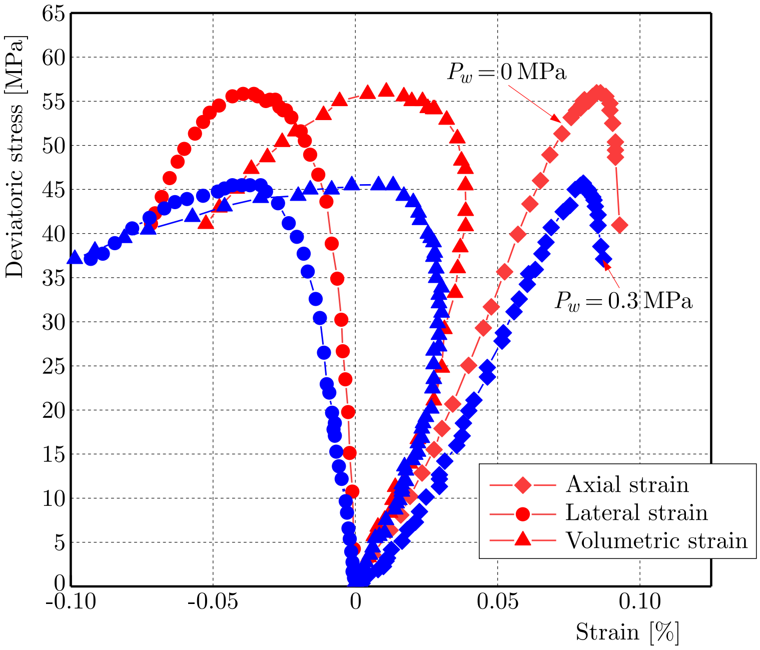

Fig. 3. Comparison of stress–strain curves for red sandstone under dry state ($P_w = 0$ MPa) and saturated-pressurized state ($P_w = 0.3$ MPa) (He *et al.*, 2026).

The intrusion of 0.3 MPa pore water pressure significantly degrades the mechanical competence of the rock. The peak compressive strength declines from 55.94 MPa to 45.69 MPa representing an 18.3 % reduction. Following the effective stress principle, the applied pore pressure counteracts the confining pressure. This interaction reduces the effective normal stress on potential failure planes and lowers the frictional resistance against shear sliding. Furthermore, the elastic modulus decreases by approximately 19 % from 22.5 GPa to 18.2 GPa. The softening indicates that water infiltration weakens the intergranular clay cementation and lubricates the grain boundaries. Additionally, the onset of dilatancy shifts from approximately 40 MPa down to 32 MPa. This critical threshold marks the initiation of unstable microcrack propagation. Consequently, the reduction significantly narrows the safe stress window for the rock mass under hydromechanical coupling.

3.2. Deformation evolution under cyclic hydraulic loading

Based on the hysteresis loops (Fig. 4) and cumulative residual strain curves (Fig. 5), the axial deformation under cyclic pore-water pressure exhibits three distinct, stress-dependent regimes:

1) Elastic shakedown regime (60 % σ_{sat}, 27.41 MPa): at this lower stress level, internal microcracks remain in a stable “breathing” state. The near-zero cumulative residual strain confirms that a 0.3 MPa hydraulic perturbation cannot overcome the frictional resistance provided by the 2 MPa confinement.
2) Plastic shakedown regime (70 % σ_{sat}, 31.98 MPa): deformation enters a self-limiting phase. The initial rapid strain accumulation (due to internal pore compaction) transitions

into a stable plateau (Fig. 5). The confining matrix effectively arrests subsequent crack propagation, leading to decreasing hysteresis loop widths (Fig. 4) as the microstructure stabilizes.

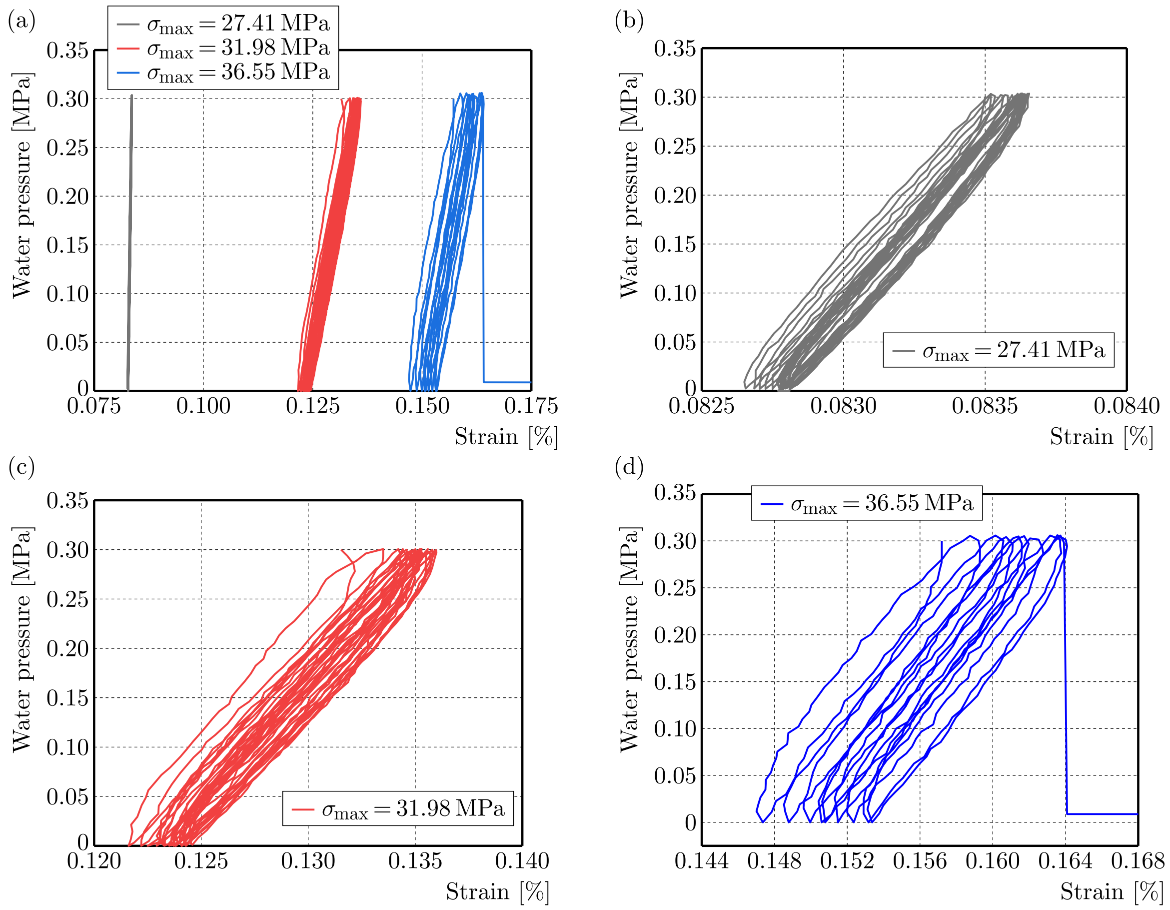

Fig. 4. Axial strain and water pressure hysteresis loops under different static axial stress levels: (a) comparative hysteresis loops; (b) 60 % of saturated peak strength 27.41 MPa; (c) 70 % of saturated peak strength 31.98 MPa; (d) 80 % of saturated peak strength 36.55 MPa.

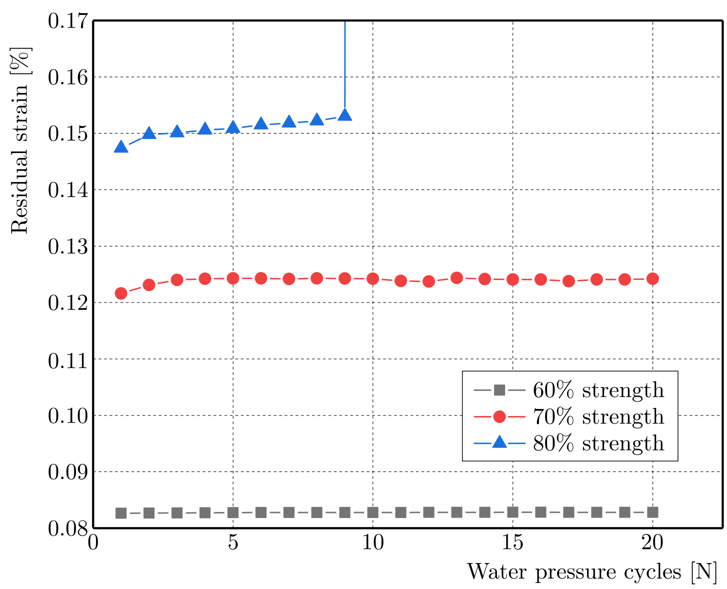

Fig. 5. Accumulation evolution of residual axial strain versus the number of pore-water pressure cycles.

3) Ratcheting and acceleration regime (80 % σ_{sat}, 36.55 MPa): approaching the dilatancy boundary, the rock transitions toward a runaway failure mode dominated by ratcheting. Hysteresis loops progressively widen and shift continuously (Fig. 4). The residual strain follows a classic three-stage fatigue trajectory, experiencing a sharp nonlinear acceleration after a critical threshold (cycles 8–10), ultimately reaching over twice the magnitude observed at the 60 % stress level by the 12th cycle.

To facilitate a clear comparison, the key experimental parameters and corresponding deformation regimes under various static stress levels are quantitatively summarized in Table 1.

Table 1. Summary of hydromechanical test parameters and resultant deformation regimes.

Axial stress level	Absolute axial stress [MPa]	Hydraulic cyclic amplitude [MPa]	Confining pressure [MPa]	Critical cycle to acceleration	Dominant deformation regime
60 % σ_{sat}	27.41	0↔0.3	2	N/A (stable)	Elastic shakedown
70 % σ_{sat}	31.98	0↔0.3	2	N/A (plateau)	Plastic shakedown
80 % σ_{sat}	36.55	0↔0.3	2	Cycles 8–10	Ratcheting

4. Energy dissipation characteristics

4.1. Calculation of energy components

Rock deformation under cyclic loading is thermodynamically an irreversible process involving energy input, accumulation, and dissipation. Based on the principle of energy conservation, the total input energy density (U) during a single loading-unloading cycle can be decomposed into elastic strain energy density (U^e) and dissipated energy density (U^d):

$$U = U^e + U^d. \tag{4.1}$$

As illustrated in Fig. 6, U corresponds to the area under the loading curve (area ABCF $= \mathrm{S}_1 + \mathrm{S}_2 + \mathrm{S}_3$), representing the total work done by the external stress field. U^e corresponds to the area under the unloading curve (area EDCF $= \mathrm{S}_2$), representing the recoverable elastic potential energy stored in the rock matrix. Consequently, the dissipated energy density U^d, which accounts for irreversible damage (e.g., microcrack propagation and frictional sliding), is calculated as the area of the hysteresis loop (area ABCDE $= \mathrm{S}_1 + \mathrm{S}_3$).

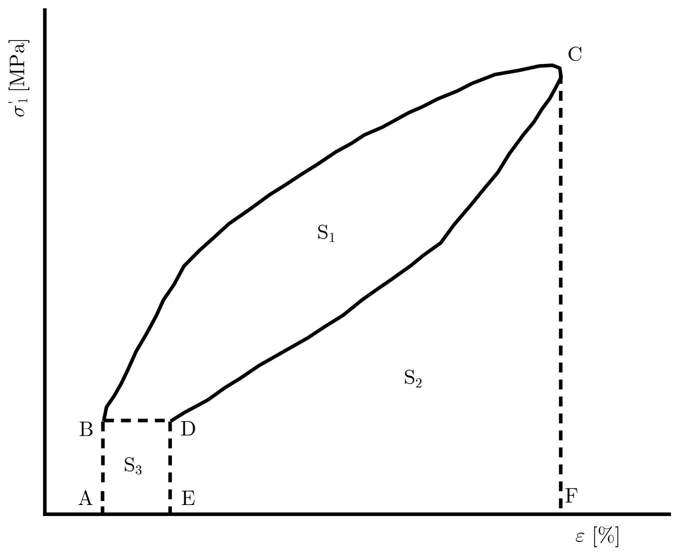

Fig. 6. Schematic diagram illustrating the calculation of elastic energy density (U^e) and dissipated energy density (U^d) from the hysteresis loop (Zhao *et al.*, 2020).

4.2. Evolution patterns of dissipated energy

The evolution of dissipated energy density (U^d) versus cycle number (Fig. 7) is strictly governed by the applied stress level, displaying a transition from two-stage to three-stage behavior:

1) Phase I: rapid adaptation (all stress levels): cycles 1–5 show a sudden drop in U^d due to a hydromechanical compaction effect, where initial pore-pressure cycles close pre-existing voids and stiffen the rock skeleton.
2) Phase II: stable dissipation (all stress levels): following initial decay, energy dissipation stabilizes. For $\sigma \leq \sigma_{\text{sat}}$, U^d remains low and constant, consumed purely by reversible friction along closed crack surfaces without new macroscopic damage.
3) Phase III: accelerated damage (only for 80 % σ_{sat}): after the 8th–10th cycle, the U^d curve uniquely turns upward at the 80 % stress level. This "U-shaped" surge indicates that energy input now exceeds the frictional dissipation capacity, driving irreversible microcrack coalescence and progressive fatigue failure.

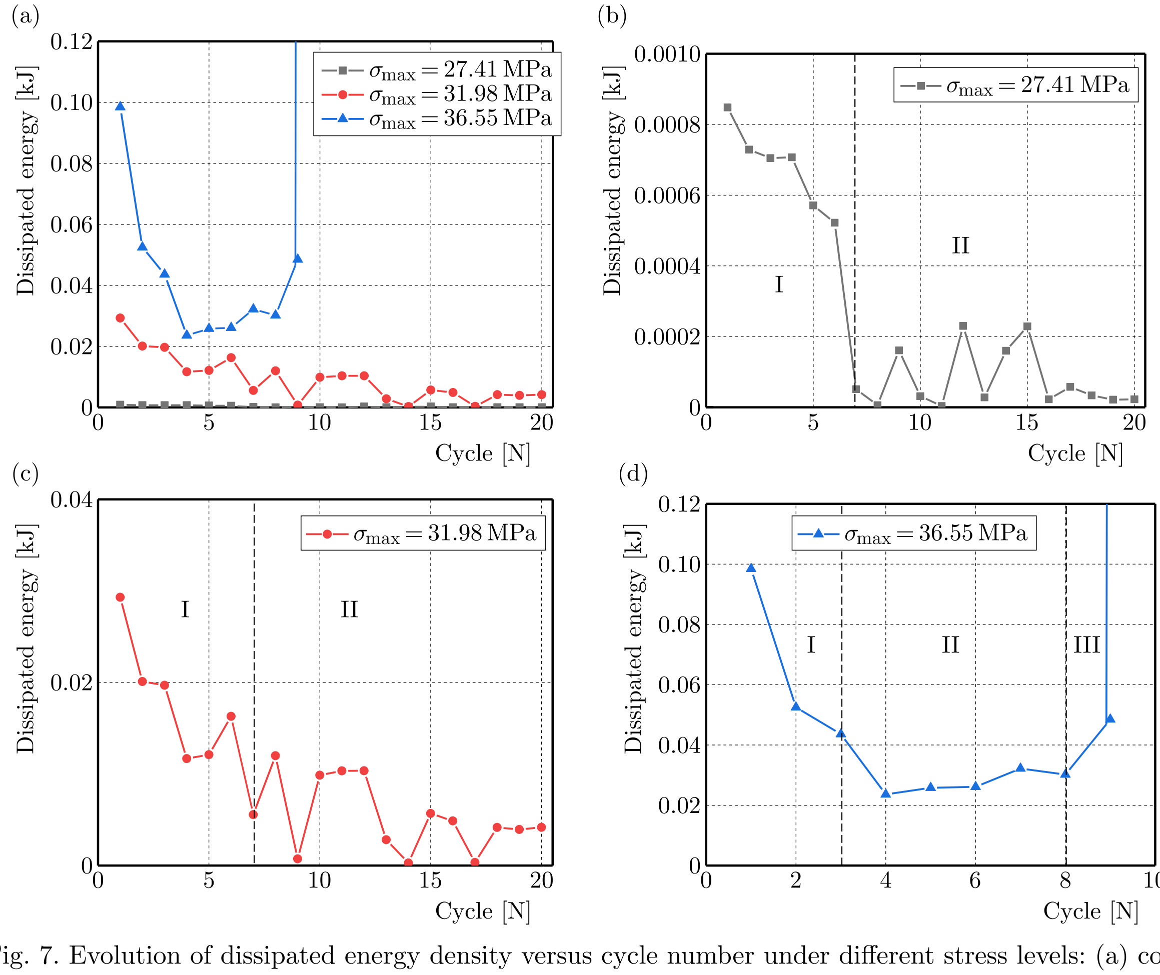

Fig. 7. Evolution of dissipated energy density versus cycle number under different stress levels: (a) comparative evolution trends; (b) 60 % of saturated peak strength (27.41 MPa); (c) 70 % of saturated peak strength (31.98 MPa); (d) 80 % of saturated peak strength (36.55 MPa).

5. Damage evolution model

5.1. Formulation of damage variable

To quantitatively characterize the hydromechanical deterioration of the saturated red sandstone, a damage variable (D) is established based on the accumulation of residual strain. According to the strain equivalence hypothesis in continuum damage mechanics (Lemaitre, 1996), the constitutive behavior of a damaged material can be represented by that of an undamaged material subjected to an effective stress. This approach is conceptually similar to Kachanov's creep rupture theory (Kachanov, 1958), where damage accumulation is intrinsically linked to the evolution of irreversible deformation. The damage variable D is typically defined as the reduction in the effective load-bearing area, which macroscopically manifests as the degradation of the elastic modulus:

$$E = E_0(1 - D), \tag{5.1}$$

where E_0 is the initial elastic modulus of the undamaged rock ($E_0 = 22.5\,\mathrm{GPa}$, derived from the monotonic test), and E is the secant modulus of the damaged rock. Under cyclic pore-water pressure loading, the total axial strain ($\varepsilon_{\mathrm{total}}$) at the peak of each cycle consists of the initial elastic strain of the rock matrix (ε_{e0}), and the cumulative irreversible strain (ε_r) resulting from internal defect propagation:

$$\varepsilon_{\mathrm{total}} = \varepsilon_{e0} + \varepsilon_r. \tag{5.2}$$

Assuming that the damaged material obeys the following constitutive relation, the total strain can be expressed as:

$$\varepsilon_{\mathrm{total}} = \frac{\sigma}{E} = \frac{\sigma}{E_0(1 - D)}. \tag{5.3}$$

For the undamaged matrix, the initial elastic strain is given by:

$$\varepsilon_{e0} = \frac{\sigma}{E_0}. \tag{5.4}$$

Substituting Eqs. (5.3) and (5.4) into Eq. (5.2) yields the relationship between residual strain and damage:

$$\varepsilon_r = \frac{\sigma}{E_0(1 - D)} - \frac{\sigma}{E_0} = \frac{\sigma}{E_0}\left(\frac{1}{1 - D} - 1\right). \tag{5.5}$$

Solving for D, we derive a practical damage quantification formula expressed solely in terms of experimentally measurable parameters (residual strain ε_r, peak stress σ, and initial modulus E_0):

$$D = \frac{\varepsilon_r E_0}{\varepsilon_r E_0 + \sigma}. \tag{5.6}$$

This result indicates that residual strain reflects the macroscopic manifestation of microscopic void growth. When $\varepsilon_r = 0$, $D = 0$ (intact state); as $\varepsilon_r \to \infty$, $D \to 1$ (failure state).

5.2. Stress-dependent damage evolution laws

The evolution of the calculated damage variable D versus cycle number N is plotted in Fig. 8. The damage trajectories reveal a distinct dependence on the applied stress ratio, demonstrating that the extent of hydromechanical deterioration is strictly controlled by the proximity of the axial stress to the rock's yield strength.

1) Stable damage state ($\sigma \le 60\,\%\ \sigma_{\mathrm{sat}}$): at the stress level of 27.41 MPa, the damage variable remains nearly constant at a low baseline level (≈ 0.35) throughout the 20 cycles. This stable plateau indicates that the hydraulic cycling at this intensity only induces reversible elastic deformation without triggering new defects. The microcracks undergo stable opening and closure ("breathing") without propagation. This behavior represents a "safe" hydromechanical state where the rock structure effectively accommodates the pore pressure fluctuations.

2) Self-limiting damage state ($\sigma = 70\%\ \sigma_{\text{sat}}$): at the intermediate stress level of 31.98 MPa, the damage curve exhibits a "step-like" increase in the first 5 cycles, rising from 0.409 to 0.414, before stabilizing. This distinct pattern suggests a self-limiting mechanism: the initial hydraulic pulses trigger local micro-adjustments and the compaction of existing voids, but the confining rock matrix provides sufficient constraint to arrest further crack extension. Consequently, the damage accumulation saturates quickly after the initial adaptation, preventing the development of macroscopic structural failure.
3) Runaway damage state ($\sigma = 80\,\%\ \sigma_{\text{sat}}$): at the high stress level of 36.55 MPa, the damage evolution undergoes a fundamental shift, following a three-stage "fatigue-creep" pattern similar to tertiary creep failure. It begins with a decelerating stage ($N = 1-2$) corresponding to initial adaptation, followed by a steady stage ($N = 2 - 10$) characterized by linear, slow damage accumulation (from 0.46 to 0.465). Crucially, an accelerating stage emerges after a critical threshold ($N > 10$), where the damage variable surges abruptly, surpassing 0.96. This sudden jump corresponds to the coalescence of distributed microcracks into a macroscopic failure plane, confirming that 80 % of the saturated strength serves as the critical stress threshold for hydraulic fatigue failure.

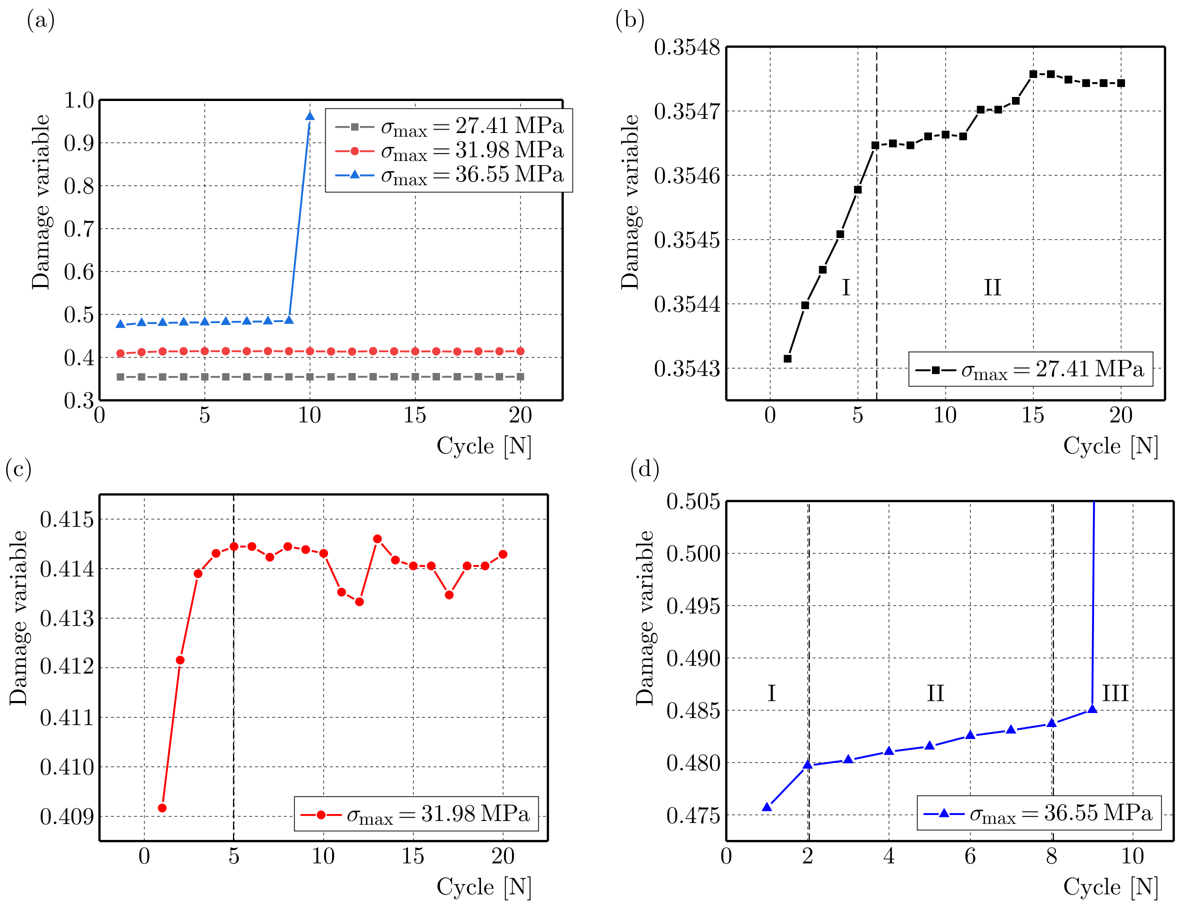

Fig. 8. Evolution of the damage variable (D) derived from residual strain under cyclic hydraulic loading: (a) comparative damage trajectories; (b) stable damage state ($\sigma = 60\%\ \sigma_{\text{sat}}$); (c) self-limiting damage state ($\sigma = 70\%\ \sigma_{\text{sat}}$); (d) runaway damage state ($\sigma = 80\%\ \sigma_{\text{sat}}$).

It is worth noting that the sudden surge in the damage variable D at the accelerating stage (Fig. 8d) aligns perfectly with the "U-shaped" upturn of dissipated energy (Fig. 7d). This consistency confirms that the derived damage model is physically grounded in the thermodynamic irreversibility of microcrack evolution.

5.3. Comparison with previous studies

The hydromechanical fatigue behavior observed in this study offers new insights distinct from traditional water-weakening protocols. To highlight the unique contribution of the current work, a comparison with existing research regarding loading paths and damage mechanisms is as follows:

1) Contrast with monotonic water-weakening: while classic static studies on water-rock interaction typically report a 15 %–30 % continuous strength degradation over long-term soaking for similar sandstones (Xuan *et al.*, 2025), our coupled dynamic tests reveal a more severe short-term degradation, recording an 18.3 % peak strength reduction upon saturation. More importantly, under monotonic loading, progressive damage only occurs with increasing shear stress. In contrast, our cyclic tests demonstrate that an extremely low dynamic fluctuation of merely 0.3 MPa can drive failure under a constant shear stress, provided the rock is held at the 80 % (σ_{sat}) threshold. This dynamic pumping effect of pore water induces fatigue damage far deeper than mere static soaking. Such a coupled mechanism significantly alters the internal pore structure and permeability evolution typically observed in similar sandstones (Wang *et al.*, 2024).
2) Distinction from high-pressure hydraulic fracturing: recent deep-earth engineering studies investigating cyclic hydraulic effects often utilize high-amplitude pressures exceeding 5 MPa to initiate new fractures (Kendrick *et al.*, 2024; Chang *et al.*, 2022). The pore pressure of 0.3 MPa applied in our study is significantly lower than the 2 MPa confinement, rendering it physically incapable of inducing hydraulic fracturing independently. Our quantitative novelty lies in establishing that this low-amplitude perturbation lowers the effective frictional resistance just enough to induce failure when the static stress is near the 70 %–80 % dilatancy boundary, which differs fundamentally from high pressure dynamic loading (Tan *et al.*, 2025) or uniaxial cyclic fatigue (Bagde & Petroš, 2005). This low amplitude fluctuation acts as a fatigue trigger rather than the primary cause of failure. It lowers the effective frictional resistance just enough to facilitate continuous slippage when the rock is already stressed near its dilatancy boundary.
3) Temporal difference from dry-wet cycling: while dry-wet cycling represents a well documented cause of reservoir bank deterioration (Yang *et al.*, 2025), it constitutes a long-term weathering process driven primarily by chemical dissolution and clay swelling over seasonal scales. The fatigue damage observed in this study operates on a much shorter meso-scale temporal domain. The rapid increase in dissipated energy and residual strain within just twenty cycles at the 80 % stress level demonstrates that intense hydraulic fluctuations during rapid reservoir regulation events can induce acute structural damage. This specific failure mode aligns with fatigue characteristics under confining pressure (Faradonbeh *et al.*, 2022) and progressive failure mechanisms reported in recent hydromechanical coupling studies (Huang *et al.*, 2025). Nevertheless, it remains fundamentally different from the slow deterioration associated with long-term weathering.

5.4. Hydromechanical fatigue mechanism

Based on the experimental data and theoretical analysis, the fatigue-like damage mechanism is summarized in Fig. 9. The cyclic pore-water pressure acts as a "hydraulic wedge" that periodically reduces the effective normal stress on crack surfaces. When coupled with the lubricating effect of water, this dynamic perturbation triggers a stress-dependent response: below the 70 % threshold, the microstructure undergoes reversible "breathing" (shakedown); whereas above the 80 % threshold, the reduced frictional resistance fails to counteract the high shear stress, leading to irreversible slip and progressive crack coalescence (ratcheting).

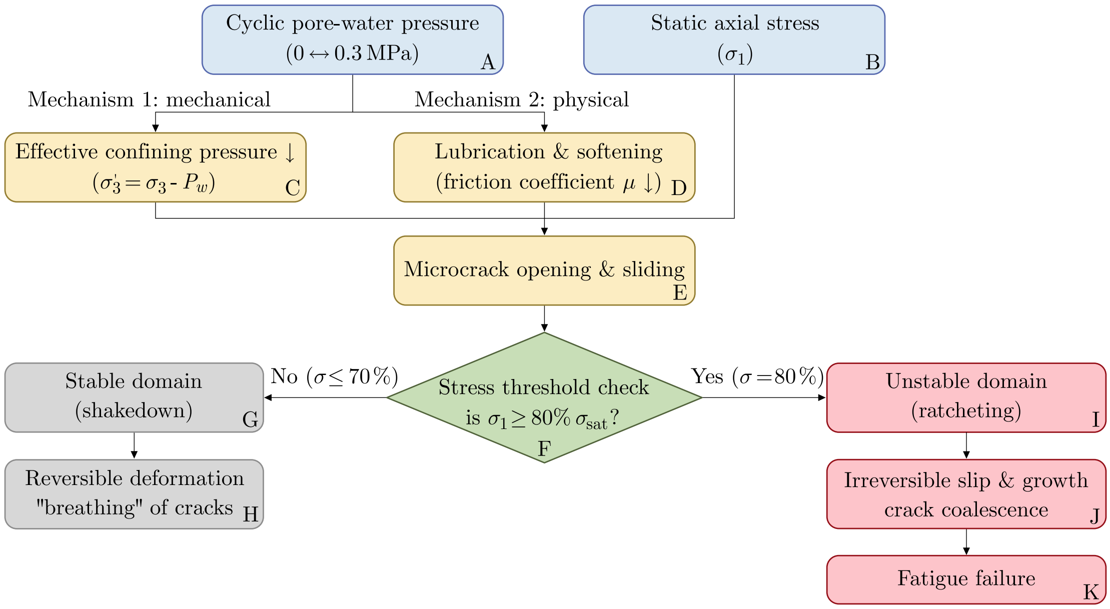

Fig. 9. Schematic diagram of the hydromechanical fatigue damage mechanism and stress-dependent threshold behaviors in saturated sandstone.

6. Conclusion

This study investigated the hydromechanical degradation and fatigue-like damage evolution of saturated red sandstone under cyclic pore-water pressure. Based on the experimental results and the derived damage model, the following conclusions are drawn:

1) The intrusion of a 0.3 MPa pore water pressure significantly weakens the mechanical competence of the red sandstone. The saturated rock exhibits an 18.3 % reduction in peak strength. This strength falls from 55.94 MPa to 45.69 MPa. The rock also shows a 19 % decline in elastic modulus compared to the dry state. This mechanical degradation stems from the dual mechanisms of effective confining pressure reduction and the physical softening of intergranular cementation. These coupled processes advance the onset of dilatancy and severely narrow the stable stress window of the rock mass.
2) The deformation response under cyclic hydraulic loading is strictly governed by the axial stress level, revealing a distinct transition from stability to failure. Specifically, within the stable domain below 32 MPa, the rock exhibits an elastic shakedown behavior. This state features stabilized damage following an initial hydromechanical adaptation. Such behavior indicates that low amplitude hydraulic cycling induces only reversible structural adjustments. Conversely, shifting to the unstable domain above 36 MPa triggers runaway damage accumulation. A critical fatigue life emerges at approximately 8–10 cycles. Beyond this specific threshold, the residual strain and dissipated energy surge nonlinearly and drive the rock toward accelerated fatigue failure.
3) A cumulative damage variable based on residual strain successfully quantifies the transition from stable crack propagation to unstable coalescence. The underlying mechanism of this hydraulic fatigue is inherently driven by the periodic fluctuation of effective stress. This dynamic fluctuation facilitates continuous frictional slippage along grain boundaries. These findings demonstrate that a critical stress threshold representing 70 % to 80 % of the saturated strength exists for reservoir bank slopes. Consequently, engineers evaluating slope stability under seasonal water level fluctuations should ensure the macroscopic factor of safety exceeds 1.4. This conservative design margin guarantees that the rock mass remains safely within the elastic shakedown domain and prevents sudden fatigue induced landslides.

Acknowledgments

This research was funded by the Graduate Innovation Program of Chongqing University of Science and Technology (grant number YKJCX2420617).

References

1. Bagde, M.N., & Petroš, V. (2005). Fatigue properties of intact sandstone samples subjected to dynamic uniaxial cyclical loading. *International Journal of Rock Mechanics and Mining Sciences*, *42*(2), 237–250. https://doi.org/10.1016/j.ijrmms.2004.08.008

2. Chang, X., Xu, E., Guo, Y., Yang, C., Hu, Z., & Guo, W. (2022). Experimental study of hydraulic fracture initiation and propagation in deep shale with different injection methods. *Journal of Petroleum Science and Engineering*, *216*, Article 110834. https://doi.org/10.1016/j.petrol.2022.110834

3. Faradonbeh, R.S., Taheri, A., & Karakus, M. (2022). Fatigue failure characteristics of sandstone under different confining pressures. *Rock Mechanics and Rock Engineering*, *55*(3), 1227–1252. https://doi.org/10.1007/s00603-021-02726-2

4. He, C.-c., Hu, X.-l., Xu, C., Wu, S.-s., Zhang, H., & Liu, C. (2020). Model test of the influence of cyclic water level fluctuations on a landslide. *Journal of Mountain Science*, *17*(1), 191–202. https://doi.org/10.1007/s11629-019-5713-9

5. He, N., Xu, J., & Zhong, W. (2026). Creep behavior and damage modeling of red sandstone under cyclic water pressure. *Advances in Civil Engineering*, *2026*(1), Article 9834337. https://doi.org/10.1155/adce/9834337

6. Hu, M., Xu, W., Wang, H., Ning, Y., Wang, R., Lyu, C., & Zhang, T. (2023). Deformation characteristics of muddy sandstones during cyclic loading and unloading with different stress lower limits under pore pressure. *International Journal of Fatigue*, *172*, Article 107606. https://doi.org/10.1016/j.ijfatigue.2023.107606

7. Huang, W., Li, Y., & Zhu, D. (2025). Mechanical characteristics and progressive failure mechanism of prefabricated defective marble under hydro-mechanical coupling. *Theoretical and Applied Fracture Mechanics*, *139*(Part B), Article 105130. https://doi.org/10.1016/j.tafmec.2025.105130

8. Kachanov, L.M. (1958). Time of the rupture process under creep conditions. *Izvestiya Akademii Nauk SSSR, Otdelenie Tekhnicheskikh Nauk*, *8*, 26–31.

9. Kendrick, J.E., Lamur, A., Mouli-Castillo, J., Lightbody, A., Fraser-Harris, A., Edlmann, K., McDermott, C.I., & Shipton, Z.K. (2024). Validating the application of cyclic hydraulic pressure pulses to reduce breakdown pressure in granite. *iScience*, *27*(10), Article 110881. https://doi.org/10.1016/j.isci.2024.110881

10. Lemaitre, J. (1996). *A course on damage mechanics* (2nd ed.). Springer.

11. Li, F., You, S., Ji, H.-g., Elmo, D., & Wang, H.-t. (2020). Strength and energy exchange of deep sandstone under high hydraulic conditions. *Journal of Central South University*, *27*(10), 3053–3062. https://doi.org/10.1007/s11771-020-4528-2

12. Li, H., Ma, L., Yang, C., Sima, Y., Liu, J., & Li, Y. (2023). Experimental investigation on the damage and deterioration of sandstone subjected to cycling pore water pressure. *Bulletin of Engineering Geology and the Environment*, *82*(4), Article 107. https://doi.org/10.1007/s10064-023-03147-x

13. Li, S., Jiao, B., Deng, B., Huang, J., & Pang, J. (2025). Impact of water–rock interaction on microstructure damage of carbonate rocks and alteration of its micromechanical properties. *Physics of Fluids*, *37*(7), Article 077104. https://doi.org/10.1063/5.0265540

14. Liang, Q., Huang, G., Zheng, J., Geng, W., Huang, J., & Sun, G. (2024). Experimental study on the response of cracked sandstone to the intermediate principal stress coupled with pore pressure. *ACS Omega*, *9*(19), 21528–21537. https://doi.org/10.1021/acsomega.4c02233

15. Liao, K., Miao, F., Wu, Y., & Zheng, H. (2025). Physical model test on a reservoir landslide with double sliding zones subjected to water level fluctuation and rainfall. *Bulletin of Engineering Geology and the Environment*, *84*(6), Article 259. https://doi.org/10.1007/s10064-025-04320-0

16. Sawicki, A., & Mierczyński, J. (2015). Some effects of intrinsic cyclic loading in saturated sands. *Journal of Theoretical and Applied Mechanics*, *53*(2), 285-293. https://doi.org/10.15632/jtam-pl.53.2.285

17. Sun, X., Ding, J., He, L., Shi, F., Zhang, Y., Miao, C., & Zhang, J. (2024). Mechanical properties and energy evolution law of water bearing sandstone under cyclic loading. *Journal of Mountain Science*, *21*(11), 3913–3929. https://doi.org/10.1007/s11629-023-8357-2

18. Tan, D., Cheng, H., Hou, C., Lei, Y., Jiang, C., Zhao, Y., & Zhang, H. (2025). Experimental study on the effects of dynamic high water pressure on the deformation characteristics of limestone. *Applied Sciences*, *15*(1), Article 42. https://doi.org/10.3390/app15010042

19. Taheri, A., Yfantidis, N., Olivares, C.L., Connelly, B.J., & Bastian, T.J. (2016). Experimental study on degradation of mechanical properties of sandstone under different cyclic loadings. *Geotechnical Testing Journal*, *39*(4), 673–687. https://doi.org/10.1520/GTJ20150231

20. Terzaghi, K. (1943). *Theoretical soil mechanics*. John Wiley & Sons.

21. Ulusay, R., & Hudson, J.A. (Eds.). (2007). *The complete ISRM suggested methods for rock characterization, testing and monitoring: 1974–2006*. ISRM Turkish National Group.

22. Wang, J., Dai, F., Yan, Z., Pang, Y., & Wei, M. (2026). Dynamic response of sandstone under hydro-mechanical coupling: macroscopic behavior and microscopic mechanism. *International Journal of Rock Mechanics and Mining Sciences*, *197*, Article 106342. https://doi.org/10.1016/j.ijrmms.2025.106342

23. Wang, M., Zhang, C., Liu, R., Bai, J., Chen, B., Sui, J., & Sun, X. (2024). Experimental study on permeability evolution of sandstone under cyclic loading. *Physics of Fluids*, *36*(4), Article 047141. https://doi.org/10.1063/5.0205903

24. Wang, W., Duan, X., Jia, Y., Bian, H., Chen, L., Zhu, Q., & Cao, Y. (2023). Damage evolution of sandstone based on acoustic emission under different seepage conditions. *European Journal of Environmental and Civil Engineering*, *27*(4), 1796–1812. https://doi.org/10.1080/19648189.2022.2098178

25. Xu, Q., Tian, A., Luo, X., Liao, X., & Tang, Q. (2022). Chemical damage constitutive model establishment and the energy analysis of rocks under water–rock interaction. *Energies*, *15*(24), Article 9386. https://doi.org/10.3390/en15249386

26. Xuan, Z., Cai, Y., Li, A., Yao, W., & Yu, J. (2025). Stress relaxation and long-term strength evaluation of water-bearing sandstone. *Mechanics of Time-Dependent Materials*, *29*(3), Article 60. https://doi.org/10.1007/s11043-025-09783-y

27. Yang, H., Liu, S., Tang, M., Xiao, X., & Cai, G. (2025). Field test study on rock mass deterioration characteristics of bank slope hydro-fluctuation belt of Three Gorges Reservoir. *Natural Hazards*, *121*(8), 8929–8950. https://doi.org/10.1007/s11069-025-07128-z

28. Zhao, B., Huang, T., Liu, D.Y., Liu, D.S., Liu, Y., & Wang, X. (2020). Experimental study and damage model study of rock salt subjected to cyclic loading and cyclic creep. *Advances in Civil Engineering*, *2020*(1), Article 8049626. https://doi.org/10.1155/2020/8049626

Manuscript received March 5, 2026; accepted for publication June 26, 2026;
published online August 22, 2026.